

RESEARCH ARTICLE

Cu–Au nanoparticles produced by the aggregation of gas-phase metal atoms for CO oxidation

*Special Issue: Emerging Investigators*Ilya V. Chepkasov¹ | Viktor S. Baidyshev² | Artem A. Golubnichiy² | Ivan S. Zamulin² | Alexander G. Kvashnin¹ | Sergey M. Kozlov³ ¹Skolkovo Institute of Science and Technology, Moscow, Russia²Katanov Khakas State University, Abakan, Russia³Department of Chemical and Biomolecular Engineering, National University of Singapore, Singapore, Singapore**Correspondence**

Sergey M. Kozlov, Department of Chemical and Biomolecular Engineering, National University of Singapore, 4 Engineering Drive 4, Singapore 117585, Singapore.
Email: cheserg@nus.edu.sg

Funding information

Agency for Science, Technology and Research (A*STAR), Grant/Award Number: LCERFI01-0033 | U2102d2006; Russian Science Foundation, Grant/Award Number: 22-23-20042

Abstract

Alloy nanoparticles (nanoalloys) are widely applied in heterogeneous catalysts, advanced electrodes, biomaterials, and other areas. The properties of nanoalloys can be tuned to a significant extent by their structures and compositions, which are governed by the employed synthetic procedure. Often such synthesis occurs in non-equilibrium conditions and yields nanoalloys with structures and properties that are different from those obtained in thermodynamic equilibrium. In this work, we characterize how the non-equilibrium conditions during the synthesis of Cu–Au alloys via physical vapor deposition (PVD) affect their morphology, composition, electronic structure, and reactivity in CO oxidation. We used molecular dynamics to simulate the PVD synthesis of Cu–Au nanoalloys through the non-isothermal aggregation of Cu and Au atoms at a 3:1 ratio in the Ar atmosphere to obtain realistic structures of Cu–Au nanoparticles. Due to the different aggregation kinetics of Au and Cu atoms, the average Au concentration in the obtained Cu–Au particles varied between 14% and 50% depending on the nanoparticle size and the aggregation time. Density functional simulations revealed that the reactivity of the obtained Cu–Au clusters toward CO and oxygen as well as Brønsted–Evans–Polanyi relations for CO oxidation significantly depend on whether the clusters had fcc, icosahedral, or amorphous structures and do not strongly correlate with the *d*-band centers of the adsorption sites. Our study highlights the importance of the non-equilibrium character of nanoalloy structure and composition for their electronic structure and catalytic properties. The performed analysis of the reactivity of Cu–Au clusters with realistic structures in CO oxidation will help the optimization of Cu–Au catalysts for this societally important reaction.

KEYWORDS

alloys, catalysis, molecular dynamics

1 | INTRODUCTION

Alloy nanoparticles (NPs, nanoalloys) are heterogeneous aggregates composed of between a few dozen and a few thousand atoms of various metals. The properties of alloy NPs are highly tunable and can be engineered to surpass the properties of pure metals.^[1–3] As a result, recent years have seen the development of many alloys for catalytic, electrochemical, structural, and other applications.^[4,5] For example, metallic Cu is one of the most active catalysts for electrochemical and thermal CO₂ reduction to valuable products such as ethylene and methanol.^[6–8] At the same time,

earlier studies revealed the propensity of Cu catalysts to be deactivated through sintering or oxidation.^[9,10] This major drawback can be eliminated by alloying Cu particles with gold, which is highly resistant to oxidation and also exhibits catalytic activity in selective oxidation^[11] and hydrogenation reactions.^[12] The obtained Cu–Au alloys exhibit very promising activity and stability in a wide variety of reactions, including CO₂ reduction, CO oxidation, and other oxidation reactions.^[13–15] Although pure Au may be also active in these reactions, depending on the oxide support chosen for Au NPs,^[15,16] alloying it with Cu provides significant cost reduction and higher flexibility in the catalyst design.

This is an open access article under the terms of the [Creative Commons Attribution](https://creativecommons.org/licenses/by/4.0/) License, which permits use, distribution and reproduction in any medium, provided the original work is properly cited.

© 2022 The Authors. *Aggregate* published by SCUT, AIEI, and John Wiley & Sons Australia, Ltd.

In general, changes in the structure, morphology, and composition of the alloy NPs are well-known^[17–19] to have a dramatic effect on their magnetic,^[20] optical,^[21] and catalytic properties.^[22] Particularly important is the relative arrangement of the components within the alloy NP, which governs its surface properties and reactivity.^[23] However, the strong dependency of the alloy properties on the NP structure also poses a challenge for the development of nanoalloy materials, which requires highly precise synthesis, characterization, and simulation techniques.^[24,25]

Synthesis of bimetallic NPs can be achieved using a wide variety of techniques, which may yield NPs with vastly different structures and properties depending on the preparation conditions.^[26] Among various techniques, chemical synthesis methods enable relatively easy preparation of nanoalloys in quantities suitable for applications, but often yield mixtures of bimetallic NPs with various sizes and with surfaces covered by ligands preventing further NP agglomeration.^[27,28] In contrast to the chemical methods, physical vapor deposition (PVD) entails the aggregation of metal atoms or tiny metal clusters in the gas phase into bigger NPs with ligand-free surfaces, which do not require additional surface treatment before application.^[29,30] The size, shape, and atomic structure of such NPs can be easily controlled by magnetron power, aggregation distance, buffer gas properties, and facile post-synthesis selection, which opens a promising way to produce nanomaterials with tightly-controlled structures.^[31,32] For example, Palmer et al. obtained Cu–Au NPs with the narrow size distribution through the aggregation of metal atoms in a helium environment.^[33] Moreover, Nguyen et al.^[34] showed that the composition of Cu–Au small particles can be controlled by changing the sputter current for each target.

In turn, precise characterization of the bimetallic NPs remains challenging, since atomic resolution is often required for the complete understanding of their properties, such as the composition of the surface layer of the alloy and its interactions with the environment.^[25] Such challenges in experimental characterization make computational studies of structure–property relations in nanoalloys particularly important.^[35] However, the reliability of computational studies strongly relies on the accuracy of the alloy models used in simulations. Usually, the design of a realistic alloy NP model is reduced to a very challenging global optimization problem, which can be tackled by a variety of methods based on evolutionary algorithms, lattice Hamiltonians, or other approaches.^[35–38] The common objective of all these methods is to identify the model that represents as closely as possible the alloy NP structure in thermodynamic equilibrium by minimizing the internal or free energy of the model. However, the immense variety of nanoalloy structures obtained experimentally suggests that the structure of alloy NPs is often governed by the synthesis procedure rather than the thermodynamic equilibrium.

Since employing realistic NP models is well-known to be extremely important for accurate description of nanostructured materials in simulations,^[39,40] various approaches were proposed to obtain representative models of the NPs prepared through the gas-phase synthesis.^[41,42] For example, the kinetic Monte Carlo model developed by Davari and Mukherjee^[43] describes the gas-phase nucleation of metallic NPs. In turn, stationary nucleation could be estimated using the mean first passage time (MFPT)^[44,45] approach. These

studies showed that an increase in the initial temperature accelerates the nucleation drastically leading to the increasing critical cluster size, which is one of the key parameters describing the overall nucleation rate.

Despite the certain success of these approaches, all dynamic features of the NP growth process can be explicitly captured only in molecular dynamics (MD) simulations. There are two main MD approaches describing gradual cooling of the system during the gas-phase synthesis of NPs. The first approach is the use of the Andersen thermostat,^[46] where the cooling of metal atoms is achieved by stochastic collisions with virtual heat bath particles. In this approach, the pressure of the buffer gas can be emulated by changing the frequency of collisions between simulated particles and the virtual Andersen particles in the box. This approach enables the simulation of condensation of $\sim 10^4$ atoms by considering in detail the nucleation, seed growth, and agglomeration.^[47–49] The results of simulations of copper condensation with Andersen imaginary heat bath well agree with the experimental data on the size, structure, and shape distribution of NPs.^[50] The second approach is based on the simulations of the condensation of NPs in the atmosphere of inert gas, such as argon. The particles cool down by colliding with buffer gas atoms, whose temperature is controlled by the Nose–Hoover thermostat.^[51,52] Since this approach is more computationally demanding, usually a relatively small number of metal atoms is included in the simulations box together with a few times higher number of buffer gas atoms.^[53–55]

Earlier studies applying this computational approach to the formation of nanoalloys explored various stages in the condensation mechanism and found that the molar ratio of formed nanoclusters corresponds well to the mole fractions of metals in the gas phase.^[29,56,57] Despite significant insights obtained in these studies on the structure of the synthesized NPs, much less is known about the mechanism of cluster seeds formation and their coagulation into NPs. More importantly, the difference between the properties of the alloy NPs synthesized in the gas phase and the corresponding NPs with equilibrium structures is yet to be characterized in the literature.

Particularly important is the investigation of the structure–property relations in Cu–Au nanoalloys, which were experimentally prepared in a wide variety of structures and morphologies. For example, the degree of order or disorder in the structure of Cu–Au nanoalloys depends on the preparation temperature and significantly affects the activity of the particles in the electrochemical CO₂ reduction and hydrogen evolution.^[58] Also, the structure of atomically precise Cu–Au nanoclusters is known to be controlled by the ligands and precursors used during the synthesis.^[59] Moreover, advanced synthesis techniques allow obtaining Cu–Au alloys as nanoboxes, or 2D materials.^[60,61] In turn, computational studies predict that the lowest-energy structures of Cu–Au nanoalloys are icosahedra with Cu@Au core@shell arrangement, which should be observed when the thermodynamic equilibrium is reached experimentally at low temperatures.^[62,63]

In this study, we simulate all stages of the gas-phase condensation of Cu–Au nanoalloys through the gas-phase aggregation of metal atoms and compare the structure, composition, and reactivity of the obtained particles to the models of core-shell and solid solution Cu–Au NPs typically studied

in the literature. In particular, we focus on the electronic structure of the alloy particles and their reactivity toward O atoms and CO molecules due to the growing scientific interest in the applications of Cu–Au alloys as CO oxidation catalysts.^[14,64] The latter reaction is particularly important for decreasing atmospheric emissions of toxic CO molecules from industrial and automotive sources.

2 | COMPUTATIONAL DETAILS

Gas-phase condensation of Cu–Au NPs in an Ar environment was studied by performing MD simulations in the LAMMPS package.^[65] Interactions between copper and gold atoms were described by EAM potentials^[66] widely used for simulations of nanostructured Cu–Au alloys.^[67] Integration of the equations of motion was performed by using the Verlet algorithm with a timestep of 2 fs over 180 ns. As the formation of NPs is exothermic, the realistic description of the heat dissipation during the simulation of the condensation process is of critical importance. In this work, we described it by explicit collisions between the metal atoms, metal particles and the buffer argon gas kept at a constant temperature of 373 K using the Nose–Hoover thermostat.^[51,52] Since argon is chemically inert, we described its interaction with copper and gold atoms by pairwise Lennard–Jones potential with $\varepsilon = 0.0123$ eV, $\sigma = 3.76$ Å.^[54]

To analyze the electronic structure and the reactivity of the NPs, we optimized the structures of individual NPs obtained from MD simulations using density functional theory (DFT).^[68,69] The generalized gradient approximation (GGA) was used with the revised Perdew–Burke–Erzenhof (PBE)^[70] parametrization for the exchange–correlation functional as implemented in the VASP software package.^[71–73] Ion–electron interaction was described by the augmented plane waves method (PAW)^[74], whose cut-off energy was set to 480 eV. The orbital occupancies were smeared using the first-order Methfessel–Paxton method with the smearing width of 0.05 eV. Grimme corrections (DFT-D3)^[75] were applied to take into account dispersive van der Waals interactions. The local geometry optimization of the cluster was conducted until the maximum force on each atom became less than 0.03 eV/Å. The transition states of CO oxidation were calculated by the climbing-image nudged elastic band method (CI-NEB).^[76] The NPs were placed in a box with a vacuum of at least 10 Å separating them. The results of the calculations were post-processed and visualized using the Open Visualization Tool (OVITO)^[77] and VESTA.^[78,79]

Adsorption energies of CO molecules and O atoms were calculated as

$$E_{\text{ads}}[\text{CO}] = E[\text{CO}/\text{Cu}_x\text{Au}_y] - E[\text{CO}] - E[\text{Cu}_x\text{Au}_y], \quad (1)$$

$$E_{\text{ads}}[\text{O}] = E[\text{O}/\text{Cu}_x\text{Au}_y] - E[\text{O}_2]/2 - E[\text{Cu}_x\text{Au}_y], \quad (2)$$

where $E[\text{CO}/\text{Cu}_x\text{Au}_y]$ and $E[\text{O}/\text{Cu}_x\text{Au}_y]$ are the energies of adsorption complexes of CO and O on Cu_xAu_y NPs, whereas $E[\text{CO}]$, $E[\text{O}_2]$, and $E[\text{Cu}_x\text{Au}_y]$ are the energies of gas-phase CO and O_2 molecules and the considered Cu_xAu_y nanoclusters, respectively.

3 | RESULTS AND DISCUSSION

3.1 | The aggregation of Cu and Au atoms in the gas phase

The Cu–Au NPs considered in this study were obtained from MD simulations of condensation of 85,000 metal atoms at the initial temperature of 2,000 K with the Cu:Au ratio of 3:1 in the atmosphere composed of 85,000 Ar atoms in a cubic box of ~ 0.2 μm in size over 180 ns. The temperature of Ar atoms was maintained at 373 K throughout the simulation using the Nose–Hoover thermostat. More parameters of the employed model and their effects on the condensation of Au and Cu atoms are discussed in the Supporting Information (Table S1, Figures S1–S5). In general, the formation of Cu–Au alloy NPs proceeds similarly to the formation of monometallic particles^[57,80,81] with significant changes in the temperature of the metal atoms in the first 100 ns when cooling by the buffer gas competes with the highly exothermic formation of tiny metal clusters.^[82–84]

The changes in the distribution of cluster sizes depending on the aggregation time are displayed in Figure 1. The condensation in the initial gas phase mixture is extremely fast with the highest number of clusters (mostly dimers and trimers) obtained after just 10 ns of atomic aggregation (Figure S5). The coagulation of smaller Cu–Au clusters into larger species starts at ~ 30 ns of the simulation as indicated by the stepwise growth of the size of the largest cluster in the mixture (Figure S5b). During the following 100 ns of the simulation, the formation of larger aggregates is observed and there are almost no single metal atoms in the mixture by $t > 100$ ns (Figure S4). At the end of the simulation at $t = 150$ ns, the average and the maximum number of atoms in clusters were 645 and 2740 atoms, respectively. Considering the average cluster size as a linear function of time, the average rates of NPs growth in our simulation can be estimated as $J = 36.5 \times 10^8$ atoms/s.

The structural analysis of the Cu–Au clusters obtained after 150 ns of the aggregation revealed that all NPs had roughly spherical shapes with 19% of them being icosahedral (Ih) and 80% of them being amorphous (Figure 1B,C, Figure S6). In addition, one of the formed clusters, $\text{Cu}_{34}\text{Au}_4$ had a “magic” fcc structure with completed atomic shells and without any low-coordinated atoms. Curiously, all icosahedral particles obtained in our simulations had between 150 and 450 atoms, although such structures are considered to be the lowest-energy structures for a much broader size range.^[62,85] We speculate that only the clusters with 150–450 atoms could obtain icosahedral structures because of their efficient cooling by the Ar atmosphere. Indeed, smaller clusters form in a highly exothermic process and require extended time to cool down and obtain low-energy structures, whereas bigger clusters require longer cooling due to their increased size.

3.2 | The composition of the formed Cu–Au aggregates

According to our simulations, only large Cu–Au clusters produced over 150 ns of the aggregation of gas-phase Cu and Au atoms have Cu:Au ratio close to 3:1 as in the initial mixture,

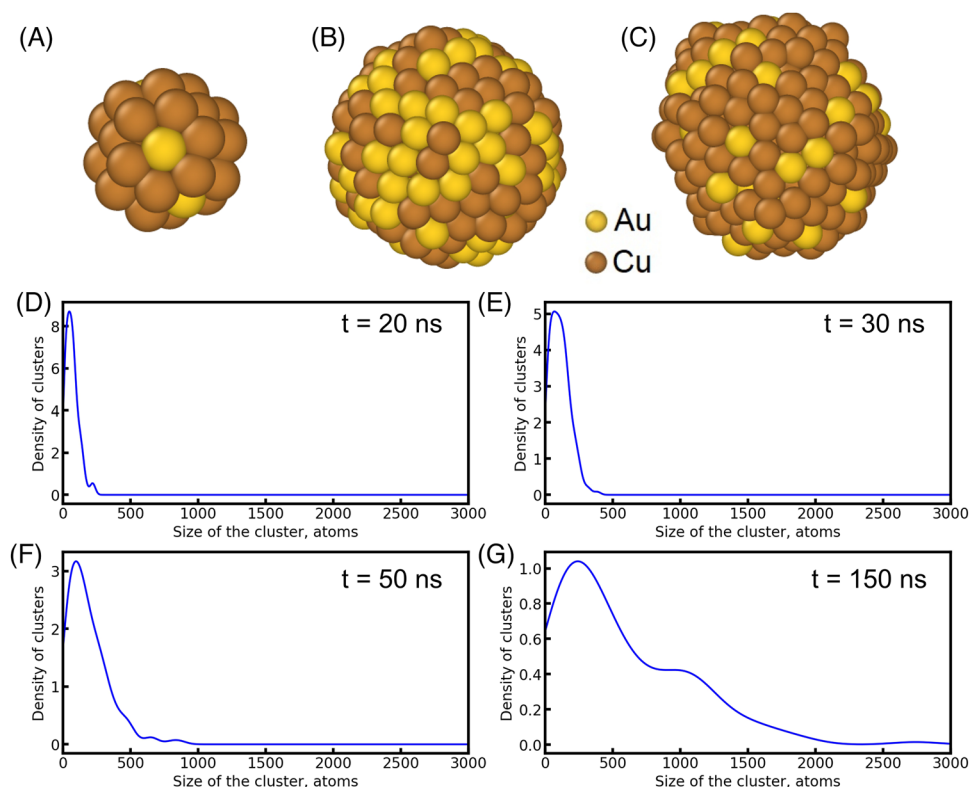


FIGURE 1 Examples of Cu–Au NPs obtained via the gas phase aggregation of Cu and Au atoms: (A) fcc Cu₃₄Au₄ (0.82 nm), (B) icosahedral Cu₂₁₀Au₉₃ (1.8 nm), (C) amorphous Cu₂₉₇Au₅₉ (2 nm). (D–G) Particle size distributions at 20, 30, 50, and 150 ns of the MD simulation

whereas the Cu:Au ratio varies significantly for smaller clusters and shorter aggregation times (Figure 2, Figure S7, Table S2). While 20 ns of condensation produce Cu–Au clusters on average enriched with Au to 40%–50% Au concentration, longer condensation times yield a mixture of larger Au-rich clusters and smaller Au-poor clusters. For example, the average Au concentration gradually increases from 25% to 39% in Cu–Au clusters over 10 atoms in size after 30 ns of condensation, whereas smaller clusters contain just 23% Au on average. After 50 ns of MD simulations, the average Au concentration in the obtained clusters gradually changes from 16% in the clusters below 10 atoms to 25% in the clusters with ~100 atoms and 32% in the biggest clusters of 400–900 atoms. Finally, by the end of the 150 ns simulation, the average Au concentration varies between 14% and 26% for NPs composed of <100 atoms and >1500 atoms, respectively, with the equilibrium 25% concentration achieved for clusters of ~1000 atoms. The concentration of Au atoms on the surface of NPs changes similarly to the overall Au concentration of Cu–Au nanoalloys (Figure S8). At $t = 150$ ns, the maximum amount of gold atoms on the surface is observed for particles with ~300 atoms, while for particles containing 500–2000 atoms the average concentration of surface Au is about 30%.

Such dependence of Au concentration on the cluster size and the condensation time can be explained by faster aggregation of Au₁ species, which completely disappear from the mixture after 50 ns compared to the 90 ns time required for the complete consumption of Cu₁ species (Figure S4). As a result of different kinetics of Au₁ and Cu₁ aggregation, the average Au concentration can reach 50% in small clusters formed at the beginning of the simulations, which serve as building blocks for Au-rich larger clusters at later stages of

the aggregation. However, the excess of Au in larger Cu–Au clusters also implies the deficit of Au in smaller Cu–Au clusters forming after 50 ns of aggregation process under a much smaller concentration of Au₁ species in the environment.

The complicated dependency between the Cu:Au ratio, the NP size, and the condensation time in our simulations as well as faster condensation of Au₁ species can be understood from the analysis of the initial stages of the atomic nucleation in dimers and trimers. According to our DFT calculations, the formation of Au₁Cu₁ clusters is 0.1 eV/atom more exothermic compared to those of Au₂ and Cu₂ clusters (Figure S9). Stable structures of mixed Au₁Cu₂ and Au₂Cu₁ clusters also have formation energies of 0.1–0.2 eV/atom more exothermic than the formation energies of monometallic Cu and Au trimers. Thus, Au concentration in the formed alloy dimers or trimers significantly exceeds 25%. Since such dimers and trimers become the building blocks for the growth of larger Cu–Au clusters, the latter also obtain elevated levels of Au for the first 100 ns of simulations. A detailed discussion of these processes in MD trajectories with various starting conditions can be found in the Supporting Information.

3.3 | The electronic structure and charge distribution in Cu–Au NPs

The alloying of Cu and Au significantly affects the electronic structure of the NPs and their surface properties. For example, CO binding energies are known to be highly sensitive to the charges on metal atoms composing the adsorption sites.^[87,88] Figure 3D shows the distribution of the average Bader^[89] charge on the surface gold atoms, the average charge on the surface copper atoms, and the average surface charge on all

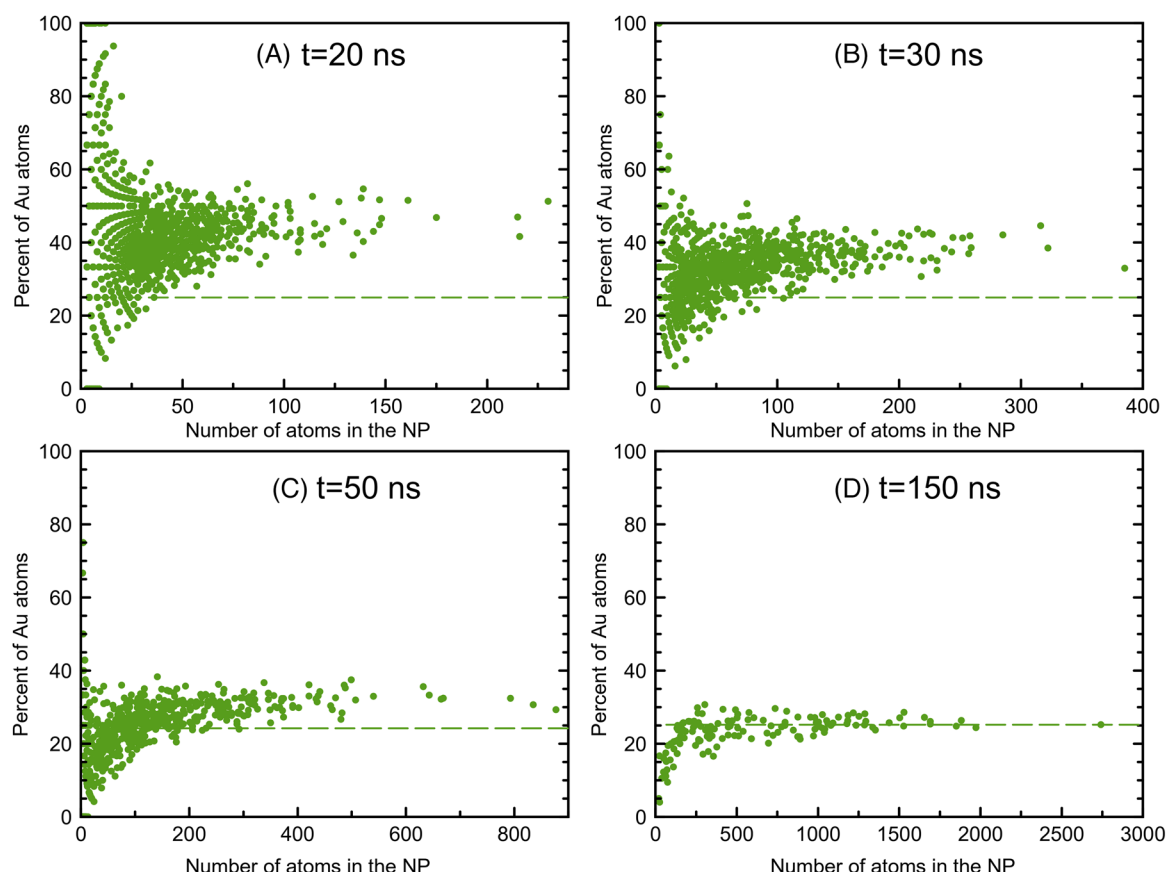


FIGURE 2 Atomic percentage of Au in NPs depending on their size after (A) 20 ns, (B) 30 ns, (C) 50 ns, and (D) 150 ns of condensation. Dashed lines denote the 25% concentration of Au in the initial mixture of metal atoms

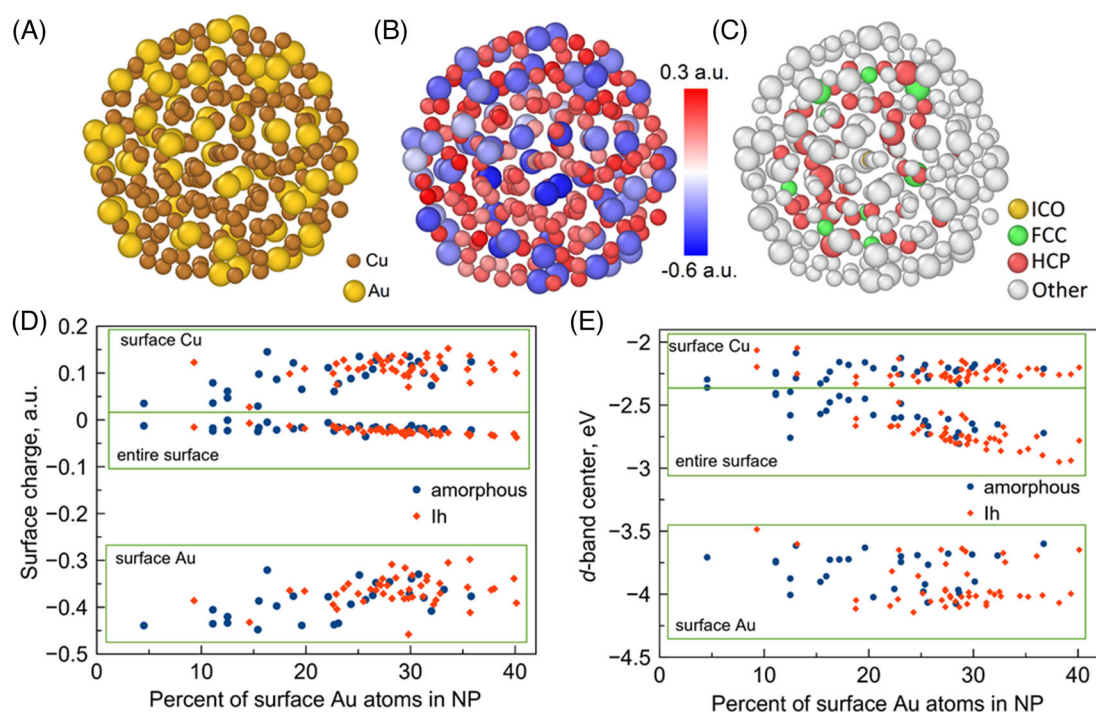


FIGURE 3 (A) The structure of the $\text{Cu}_{196}\text{Au}_{68}$ particle obtained at the end of the MD simulation, (B) charge distribution in the $\text{Cu}_{196}\text{Au}_{68}$ NP, (C) common neighbor analysis (CNA)^[86] of the $\text{Cu}_{196}\text{Au}_{68}$ NP, (D) atomic charges averaged over the surface Cu and Au atoms as well as all surface atoms depending on the Au concentration in the obtained NPs with icosahedral and amorphous structures, (E) d -band centers averaged over surface Cu and Au atoms as well as all surface atoms depending on the Au concentration in the NPs with icosahedral and amorphous structures obtained in the MD simulation

particles. For both icosahedral and amorphous NPs, surface Cu atoms are calculated to obtain a charge between +0.007 and +0.152 a.u. due to Cu–Au charge transfer, whereas surface Au atoms obtain charge between −0.298 and −0.458 a.u. Notably, Au atoms obtain more negative charges in Au-poor clusters, whereas Cu atoms obtain more positive charges in the clusters with a higher Au concentration. The direction and the magnitude of the charge transfer can be explained by the 0.4 eV higher work function of Au compared to Cu^[90] and a higher concentration of Cu than Au in the obtained NPs. Despite this pronounced charge redistribution, the average surface charge remains close to zero on all NPs. Note that such a degree of charge transfer was concluded not to affect the accuracy of the interatomic potentials for Cu–Au nanoalloys.^[62]

Curiously, the center of *d*-bands in the electronic densities of states projected on surface atoms vary in a different way with Au concentration in the clusters compared to the Bader charges. For example, *d*-band centers of surface Cu atoms are located around −2.3 eV below the Fermi level, irrespective of the Au concentration in the cluster. In turn, *d*-band centers of surface Au atoms vary between −3.6 and −4.1 eV below the Fermi level but depend more on the structure of the cluster rather than its composition. Namely, the average positions of the *d*-band center of surface Au atoms in the average (median) icosahedral Cu–Au cluster is calculated to be 0.1 eV (0.26 eV) deeper below the Fermi level compared to those in amorphous Cu–Au clusters. Although the *d*-band centers of surface Cu and Au atoms do not significantly depend on the particle composition, the average *d*-band center of all surface atoms changes with composition from −2.4 eV for clusters with a minimal amount of Au to −2.8 eV for Cu–Au clusters with Au concentration around 40%.

3.4 | The catalytic activity of Cu–Au NPs

The changes in the electronic structure of Cu–Au NPs caused by the alloying and their formation in conditions far away from thermodynamic equilibrium have profound implications for their catalytic activity. We illustrate this by evaluating the interactions of the obtained Cu–Au particles with CO molecules and O atoms, which are the key species in CO oxidation on Cu–Au catalysts. We focus on the latter reaction as one of the most societally important reactions for air quality control and is also one of the most studied reactions in heterogeneous catalysis.^[91] Although the elementary reaction of CO with surface oxygen via Langmuir–Hinshelwood or Eley–Rideal mechanisms can be as low as 0.2–0.3 eV on Cu^[92–94] and other transition metal catalysts,^[95,96] the availability of surface oxygen may be insufficient to achieve the high reaction rate. Whereas some catalysts like Au may require some promotion to activate O₂ molecules,^[97,98] the application of most CO oxidation catalysts is complicated by their facile CO poisoning, which deactivates them at room and moderate temperatures. CO poisoning occurs due to insufficient coverage of surface O caused by the competitive adsorption of oxygen and CO molecules on the catalyst surface, which is governed by the difference between their adsorption energies.^[99] Thus, the binding strength of the catalyst with respect to CO and oxygen is essential to describe CO oxidation kinetics.

Cu–Au alloy NPs expose numerous nonequivalent adsorption sites with various compositions and widely diverse structures formed during the non-equilibrium aggregation of Cu and Au atoms from the gas phase. Since the explicit analysis of the adsorption properties of these sites is a very computationally demanding task, we performed it for three representative cluster structures obtained from MD simulations. Namely, we considered Cu₃₄Au₄ clusters with fcc structure as well as icosahedral Cu₅₀Au₆ and amorphous Cu₅₆Au₇ clusters. Note that all of these clusters consist of ~11% Au despite 25% of Au in the mixture of metal atoms at the beginning of the aggregation, since all clusters with similar size had Au-poor composition. The considered Cu₅₀Au₆ and Cu₅₆Au₇ clusters also have very similar sizes of 1 nm facilitating the direct comparison of their properties, whereas the Cu₃₄Au₄ cluster is a bit smaller, 0.8 nm. The latter cluster was chosen as the only cluster with the fcc structure formed in the aggregation process due to its “magic” size that avoids the formation of low-coordinated atoms.

The binding energies of O atoms and CO molecules to various sites of these clusters are summarized in Figure 4, whereas representative structures of the O and CO on Cu–Au clusters are displayed in Figures S12–S14 in the Supporting Information. One can see that purely Cu sites bind O and CO more strongly compared to mixed Cu–Au sites on all clusters, whereas purely Au sites are not locally stable for the adsorption of these species. More interesting is the dependence of the calculated adsorption energies on the structure of the considered NPs. For example, Cu₃₄Au₄ clusters with fcc structure feature Cu₃ binding sites with the strongest O binding, whereas O binding on mixed Au₁Cu₂ sites is calculated to be the strongest on the amorphous Cu₅₆Au₇ cluster. In turn, the icosahedral Cu₅₆Au₇ does not expose surface sites with strong O binding energies. Nevertheless, the latter cluster exposes the sites with the strongest binding of CO molecules, which prefer to adsorb on Cu₂ bridge sites on these clusters. Although the binding energies of CO molecules on amorphous Cu₅₆Au₇ and fcc Cu₃₄Au₄ are calculated to be similar, one could notice that only the former can adsorb CO on mixed Au₁Cu₂ sites, whereas only the latter can provide Cu₄ sites for CO adsorption.

To get more insights into the effects of the structure and composition of Cu–Au nanoclusters on their reactivity, we calculated CO and O adsorption energies on fcc, icosahedral, and amorphous clusters with altered compositions and distributions of elements (Figure 5). Namely, we considered these clusters with purely Cu or purely Au compositions as well as Cu@Au and Au@Cu core-shell structures. Note that the considered fcc, icosahedral, and amorphous clusters contain 84%, 77%, and 76% of atoms on their surface, respectively, which affected the composition of the clusters with core-shell structures. Our results show that O binding energies on Cu–Au clusters obtained in MD simulations are similar to the O binding energies calculated on pure Cu or Au@Cu core-shell nanoclusters, although the distribution of the binding energies is significantly wider for the former cluster. Clusters composed of pure Au and clusters with Cu core and Au shell bind O atoms significantly weaker than Cu–Au clusters obtained in the aggregation process. Curiously, the structural properties of the clusters strongly affect O binding energies also on purely Au and core-shell Cu–Au clusters. For example, the average binding energies of O atoms are

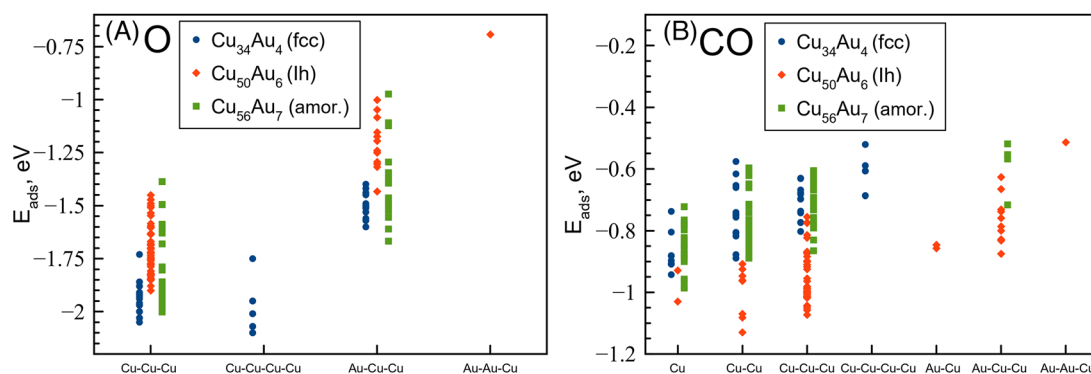


FIGURE 4 Binding energies of (A) O atoms and (B) CO molecules to the considered Cu–Au clusters for various compositions of the adsorption sites

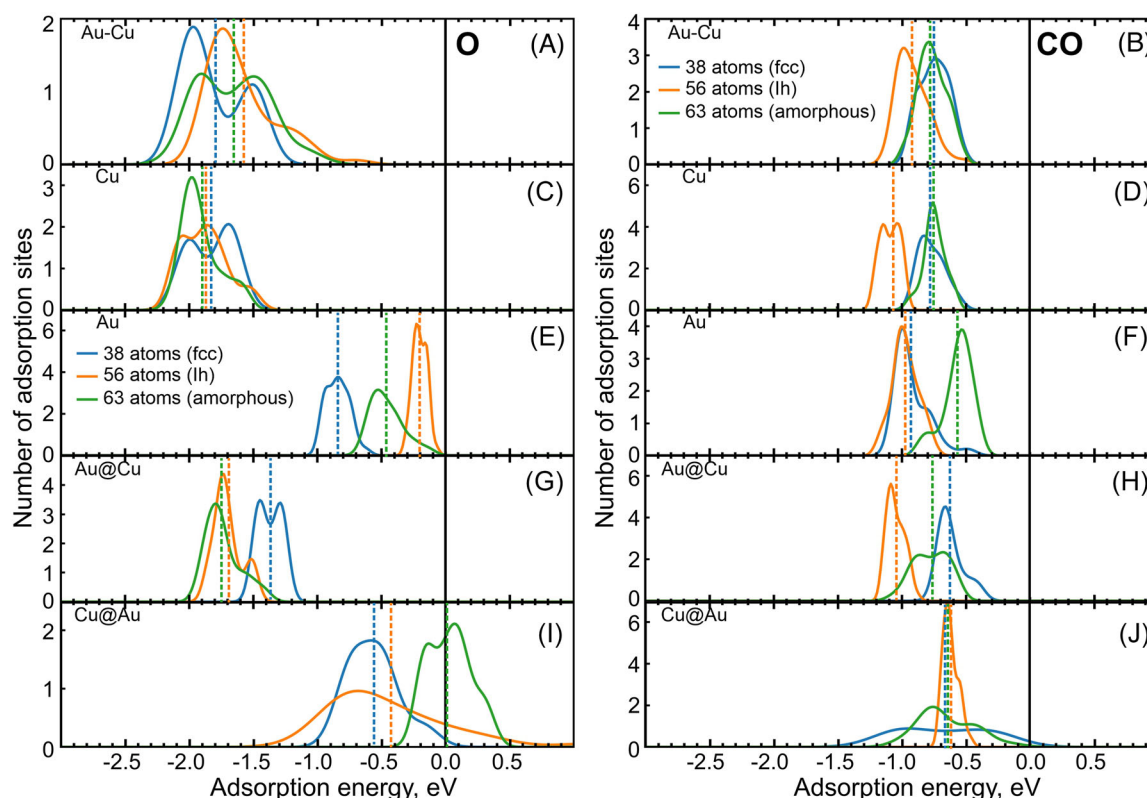


FIGURE 5 Distributions of adsorption energies of O and CO species calculated for (A, B) fcc, $\text{Cu}_{34}\text{Au}_4$ icosahedral, $\text{Cu}_{50}\text{Au}_6$ and amorphous $\text{Cu}_{56}\text{Au}_7$ clusters from MD simulations; (C, D) the same cluster structures composed of pure Cu; (E, F) the same cluster structures composed of pure Au; (G, H) the same cluster structures, in which Au atoms compose the core and Cu atoms compose the shell; (I, J) the same cluster structures, in which Cu atoms compose the core and Au atoms compose the shell. The distributions were obtained by applying 0.35 eV smearing to the calculated adsorption energies. The dashed lines reflect average adsorption energies calculated for each distribution

0.38 and 0.59 eV more exothermic on clusters with fcc structure composed of pure Au, or with Cu@Au core@shell structure compared to the respective clusters with an amorphous structure. As a result, O binding energies calculated on purely Au cluster with fcc structure are only slightly less endothermic than those on the same cluster with Au-core Cu-shell structure, despite the completely different composition of the adsorption sites. Although O atoms are calculated to bind with similar strength to icosahedral and amorphous Cu–Au clusters obtained from MD or with Cu-core Au-shell structure, the binding is much stronger to amorphous structures for pure Au composition and significantly stronger to icosahedral clusters for Cu@Au core@shell particles.

In turn, CO binding energies are calculated to be much more sensitive to the structure of the Cu–Au clusters than to their composition, because of the relatively similar adsorption strength of CO on pure Cu and pure Au. Figure 5 shows that icosahedral clusters composed of pure Cu, pure Au or with Au-core Cu-shell composition adsorb CO molecules notably stronger than other clusters. Moreover, icosahedral clusters with Cu@Au core@shell composition show a much narrower distribution of CO binding energies compared to fcc and amorphous clusters. In turn, amorphous clusters bind CO molecules more weakly than fcc clusters for pure Au composition, but more strongly for the clusters with Au core and Cu shell. Overall, the adsorption properties are

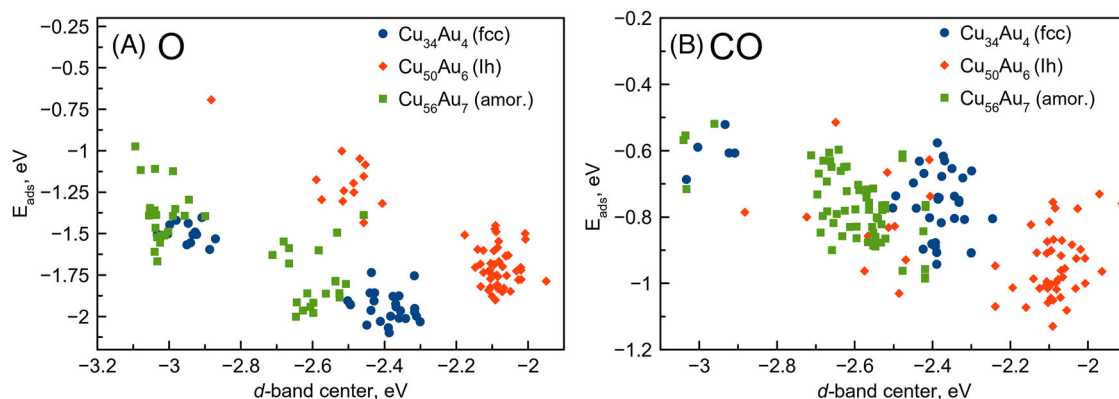


FIGURE 6 Correlation of (A) O and (B) CO adsorption energies with the d -band center of the electronic density of states projected on atoms composing the site for fcc $\text{Cu}_{34}\text{Au}_4$, icosahedral $\text{Cu}_{50}\text{Au}_6$, and amorphous $\text{Cu}_{56}\text{Au}_7$ clusters

calculated to strongly depend on the cluster structures in a hard-to-predict manner.

Such dependency of the adsorption energies calculated on the fcc, icosahedral, and amorphous cluster structure is hard to rationalize by the differences in the positions of d -band centers calculated for their surface atoms at -2.54 , -2.20 , and -2.76 eV below the Fermi level, respectively (Figure 6). The representative electronic densities of states are displayed in Figures S12 and S13 in the Supporting Information. In general, our results show that the binding energies of O atoms on CO molecules to Cu–Au clusters become less exothermic with increasing depth of their d -bands below the Fermi level, which agrees well with trends in previous studies.^[100] However, the differences between binding energies of O atoms to icosahedral $\text{Cu}_{50}\text{Au}_6$ and other clusters are much smaller than what would be expected from the differences between the respective d -band centers of the adsorption sites. Note that the considered $\text{Cu}_{50}\text{Au}_6$ is not the only icosahedral cluster with a less negative position of the d -band center (Figure 3E). Moreover, CO binding energies on $\text{Cu}_{56}\text{Au}_7$ are virtually the same as on fcc $\text{Cu}_{34}\text{Au}_4$ clusters despite a notable shift in their d -band center positions. Thus, the structure of the clusters is calculated to introduce significant deviations into the well-established correlation between the adsorption properties of the sites and the positions of their d -band centers, which is widely used for the rational design and analysis of heterogeneous catalysts.^[101] Note that the average charge on the metal atoms composing the adsorption sites roughly follows the composition of the sites and does not provide significant additional insight into their binding properties (Figure S10).

Although the direct calculation of the catalytic activity of the obtained Cu–Au NPs in CO oxidation appears hardly possible due to the significant number of nonequivalent sites on their surfaces, their activity can be evaluated through Brønsted–Evans–Polanyi (BEP) relations.^[102,103] These relations postulate that the activation and reaction energies for a given elementary step linearly correlate with each other within a certain family of catalytic materials (e.g., transition metals or oxides). In principle, the validity of such relations is well-established for regular alloy surfaces,^[104,105] whereas their applicability to NPs and amorphous materials is less explored.^[106,107]

To construct the BEP relations for the considered Cu–Au clusters, we calculated the activation energies for oxidation of physisorbed CO molecules by chemisorbed O atoms on

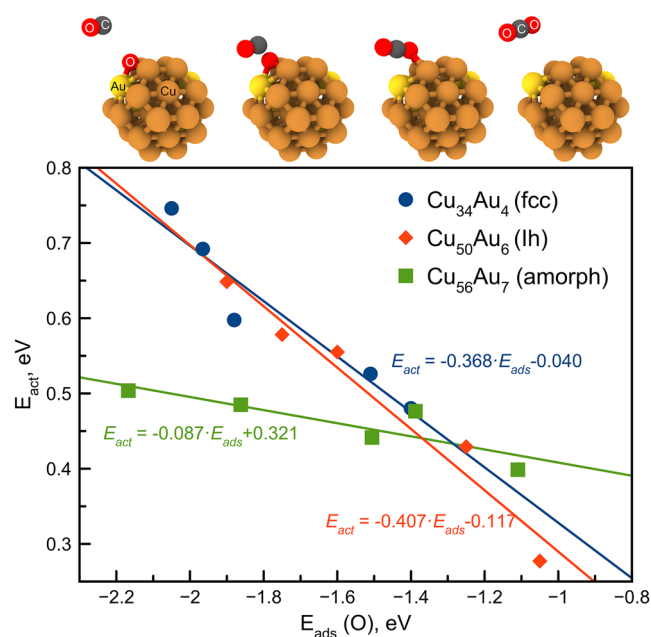


FIGURE 7 The correlation between adsorption energy of oxygen and activation energy of CO oxidation step. A schematic illustration of the considered reaction is shown at the top panel for fcc $\text{Cu}_{34}\text{Au}_4$ cluster

the catalyst surface via the Eley–Rideal mechanism. Note that the considered reaction mechanism involves gas-phase CO and CO_2 species as well as O atoms bound to the catalyst surface. Thus, the reaction energy of this process is fully controlled by the O binding energy to the catalyst surface. We calculated the CO oxidation barriers for five surface sites on each of the considered Cu–Au clusters, fcc $\text{Cu}_{34}\text{Au}_4$, icosahedral $\text{Cu}_{50}\text{Au}_6$, and amorphous $\text{Cu}_{56}\text{Au}_7$. The considered five sites were chosen to exhibit significant differences between binding energies of O atoms and reaction energies of CO oxidation on them to increase the breadth of the sampling and the statistical reliability of the BEP analysis. In general, the reaction and activation energies of the CO oxidation step correlated well for every considered Cu–Au cluster, validating the BEP approach for these systems (Figure 7). However, on icosahedral and fcc clusters the activation energies were calculated to vary significantly from 0.75 eV on strongly binding sites to 0.3 eV on weakly binding sites, whereas the activation energies on the amorphous Cu–Au clusters barely changed among all the considered sites. As a result,

significantly different expressions for BEP relations were obtained for amorphous clusters compared to those of fcc and icosahedral clusters, which imply significantly different trends in the catalytic activity of the former.

Importantly, the obtained BEP relations show that the rate of CO oxidation on fcc and icosahedral clusters can be dramatically accelerated by lower activation energies on surface sites with weak O binding. Since O binding energies on Cu–Au alloys are on average weaker than on pure Cu (Figure 5A,C), our calculations predict a remarkable effect of alloying on the catalytic activity of Cu particles, which depends on the cluster structure. We can roughly estimate the CO oxidation rate on the clusters from their BEP relations and O binding energies averaged over all surface sites. Whereas alloying Cu with Au is calculated to increase the rate constant of CO oxidation ~ 40 times at room temperature on icosahedral clusters, the increase will be only ~ 2.5 times on fcc and amorphous clusters, due to virtually unchanged O binding energies or low sensitivity of the reaction rate to O binding energies, respectively.

Note that this analysis did not consider coverage effects and was based on the assumption that all surface sites catalyze CO oxidation independently of each other. However, CO oxidation is inherently a multi-site reaction, where sites are entangled through the propagation of activation and deactivation fronts between O and CO-covered areas.^[91,108] Moreover, different sites on the alloy surface may be responsible for O₂ activation and CO oxidation steps, which could significantly affect the catalytic activity but was not accounted for in the present analysis. Systematic studies of multi-site reactions require kinetic Monte-Carlo simulations, whose application to nanoparticulate and amorphous catalysts is currently under intense development.^[109,110]

4 | CONCLUSIONS

In summary, we obtained realistic structures of Cu–Au NPs through the MD simulations of the non-isothermal gas-phase aggregation of hot Cu and Au atoms in Ar gas kept at 373 K. Since the aggregation of Cu and Au atoms occurs under conditions far away from the thermodynamic equilibrium, the obtained cluster structures and compositions differ significantly from those in previous studies, which mostly considered low-energy cluster structures. For example, faster formation of heteroatomic dimers and trimers compared to monometallic Cu and Au species in the reaction mixture with a 3:1 Cu:Au ratio leads to Au-rich compositions of the Cu–Au clusters formed in the first 50 ns of aggregation. In turn, the fast depletion of Au₁ species in the reaction mixture decreases Au concentration in smaller Cu–Au clusters formed later in the aggregation process.

Density functional calculations of the clusters obtained from MD simulations revealed that each surface Cu atom may donate up to 0.15 electrons to Au atoms, which obtain charges up to -0.46 a.u. on the cluster surface. Moreover, the electronic structure and the reactivity of the clusters towards CO molecules and O atoms are found to depend strongly on the non-equilibrium character of their structures, which can be fcc, icosahedral, or amorphous. We found that Cu–Au clusters with different structure types produced during the aggregation expose different types of locally stable

sites for CO and O adsorption. The adsorption properties of Cu–Au clusters varied in a complicated fashion among fcc, icosahedral, and amorphous structures, which introduced deviations in the correlation between the adsorption energies and the electronic structure (*d*-band center) of the active sites. Moreover, CO adsorption energies on Cu–Au clusters were found to be more sensitive to the cluster structure than to the composition of the adsorption site or the cluster, in general. Curiously, the Brønsted–Evans–Polanyi relations between activation and reaction energies of CO oxidation by adsorbed O atoms calculated on amorphous Cu–Au clusters were markedly different from those on fcc and amorphous clusters. These variations of CO and O adsorption energies and BEP relations on Cu–Au clusters are extremely important for the description of the CO oxidation activity of Cu–Au catalysts, which is shown to be highly sensitive to the structure of the obtained Cu–Au NPs and, hence, the conditions of their synthesis.

In general, this study revealed significant differences between the electronic structures and the reactivities calculated for the cluster models obtained in MD simulations and the simplified alloy cluster models typically used in density functional studies. Hence, employing realistic models of cluster structures is concluded to be essential for performing accurate simulations of the catalytic properties of nanostructured metals and alloys. Since NP structures obtained experimentally may be far away from the thermodynamic equilibrium, such realistic models can be obtained only by closely mimicking synthesis conditions in simulations, for example, by performing thorough MD simulations of the aggregation of metal atoms. The strong dependency of CO oxidation activity on the structure of Cu–Au clusters established in this study using realistic models will help further experimental efforts to optimize Cu–Au catalysts for this societally important reaction.

ACKNOWLEDGMENTS

The authors are grateful to Zakhar I. Popov for the discussion. The research is carried out using resources of the Center for the Information and Computing of Novosibirsk State University. Calculations of transition states and energy barriers were carried out on the *ElGatito* supercomputer of the Industry-Oriented Computational Discovery group at the Skoltech Project Center for energy Transition and ESG.

CONFLICT OF INTEREST

The authors declare that there is no conflict of interest that could be perceived as prejudicing the impartiality of the research reported.

ORCID

Sergey M. Kozlov  <https://orcid.org/0000-0002-7765-4649>

REFERENCES

1. A. Sápi, T. Rajkumar, J. Kiss, Á. Kukovecz, Z. Kónya, G. A. Somorjai, *Catal. Lett.* **2021**, *151*, 2153.
2. J. E. van der Hoeven, J. Jelic, L. A. Olthof, G. Totarella, R. J. van Dijk-Moes, J.-M. Krafft, C. Louis, F. Studt, A. van Blaaderen, P. E. de Jongh, *Nat. Mater.* **2021**, *20*, 1216.
3. X. Huang, O. Akdim, M. Douthwaite, K. Wang, L. Zhao, R. J. Lewis, S. Pattison, I. T. Daniel, P. J. Miedziak, G. Shaw, D. J. Morgan, S. M. Althahban, T. E. Davies, Q. He, F. Wang, J. Fu, D. Bethell, S. McIntosh, C. J. Kiely, G. J. Hutchings, *Nature* **2022**, *603*, 271.

4. J. K. Pedersen, T. A. Batchelor, D. Yan, L. E. J. Skjogstad, J. Rossmeisl, *Curr. Opin. Electrochem.* **2021**, *26*, 100651.
5. J. Qiao, Q. Wang, J. Pelletier, H. Kato, R. Casalini, D. Crespo, E. Pineda, Y. Yao, Y. Yang, *Prog. Mater. Sci.* **2019**, *104*, 250.
6. Z. Weng, Y. Wu, M. Wang, J. Jiang, K. Yang, S. Huo, X.-F. Wang, Q. Ma, G. W. Brudvig, V. S. Batista, Y. Liang, Z. Feng, H. Wang, *Nat. Commun.* **2018**, *9*, 415.
7. Z. Weng, J. Jiang, Y. Wu, Z. Wu, X. Guo, K. L. Materna, W. Liu, V. S. Batista, G. W. Brudvig, H. Wang, *J. Am. Chem. Soc.* **2016**, *138*, 8076.
8. H. Iwai, T. Umeki, M. Yokomatsu, C. Egawa, *Surf. Sci.* **2008**, *602*, 2541.
9. M. B. Gawande, A. Goswami, F.-X. Felpin, T. Asefa, X. Huang, R. Silva, X. Zou, R. Zboril, R. S. Varma, *Chem. Rev.* **2016**, *116*, 3722.
10. Y. i. Hori, *Modern Aspects of Electrochemistry*, pp. 89–189. Springer, **2008**.
11. G. C. Bond, C. Louis, D. Thompson, *Catalysis by Gold*, vol. 6, World Scientific, **2006**.
12. A. Corma, H. Garcia, *Chem. Soc. Rev.* **2008**, *37*, 2096.
13. S. Neatu, J. A. Macia-Agullo, P. Concepcion, H. Garcia, *J. Am. Chem. Soc.* **2014**, *136*, 15969.
14. X. Liu, A. Wang, X. Wang, C.-Y. Mou, T. Zhang, *Chem. Commun.* **2008**, *27*, 3187.
15. C. L. Bracey, P. R. Ellis, G. J. Hutchings, *Chem. Soc. Rev.* **2009**, *38*, 2231.
16. T. Ishida, T. Murayama, A. Taketoshi, M. Haruta, *Chem. Rev.* **2019**, *120*, 464.
17. R. Ferrando, J. Jellinek, R. L. Johnston, *Chem. Rev.* **2008**, *108*, 845.
18. M. Fèvre, Y. Le Bouar, A. Finel, *Phys. Rev. B* **2018**, *97*, 195404.
19. J. Li, G. Wang, G. Zhou, *Surf. Sci.* **2016**, *649*, 39.
20. H. Zeng, S. Sun, J. Li, Z. Wang, J. Liu, *Appl. Phys. Lett.* **2004**, *85*, 792.
21. K. J. Major, C. De, S. O. Obare, *Plasmonics* **2009**, *4*, 61.
22. E. A. Redina, A. A. Greish, I. V. Mishin, G. I. Kapustin, O. P. Tkachenko, O. A. Kirichenko, L. M. Kustov, *Catal. Today* **2015**, *241*, 246.
23. N. Lasemi, G. Rupprechter, *Catalysts* **2020**, *10*, 1453.
24. K. Loza, M. Heggen, M. Epple, *Adv. Funct. Mater.* **2020**, *30*, 1909260.
25. J. D. Lee, J. B. Miller, A. V. Shneidman, L. Sun, J. F. Weaver, J. Aizenberg, J. Biener, J. A. Boscoboinik, A. C. Foucher, A. I. Frenkel, J. E. S. van der Hoeven, B. Kozinsky, N. Marcella, M. M. Montemore, H. T. Ngan, C. R. O'Connor, C. J. Owen, D. J. Stacchiola, E. A. Stach, R. J. Madix, P. Sautet, C. M. Friend, *Chem. Rev.* **2022**, *122*, 8758.
26. H.-H. Li, S.-H. Yu, *Adv. Mater.* **2019**, *31*, 1803503.
27. X. Wang, J. Zhuang, Q. Peng, Y. Li, *Nature* **2005**, *437*, 121.
28. H. Wang, L. Chen, Y. Feng, H. Chen, *Acc. Chem. Res.* **2013**, *46*, 1636.
29. V. Singh, C. Cassidy, P. Grammatikopoulos, F. Djurabekova, K. Nordlund, M. Sowwan, *J. Phys. Chem. C* **2014**, *118*, 13869.
30. M. A. Koten, S. Voeller, M. Patterson, J. E. Shield, *J. Appl. Phys.* **2016**, *119*, 114306.
31. D. König, K. Richter, A. Siegel, A.-V. Mudring, A. Ludwig, *Adv. Funct. Mater.* **2014**, *24*, 2049.
32. S. Suzuki, Y. Tomita, S. Kuwabata, T. Torimoto, *Dalton Trans.* **2015**, *44*, 4186.
33. F. Yin, Z. W. Wang, R. E. Palmer, *J. Am. Chem. Soc.* **2011**, *133*, 10325.
34. M. T. Nguyen, H. Zhang, L. Deng, T. Tokunaga, T. Yonezawa, *Langmuir* **2017**, *33*, 12389.
35. R. Ferrando, *J. Nanopart. Res.* **2018**, *20*, 1.
36. S. M. Kozlov, G. Kovács, R. Ferrando, K. M. Neyman, *Chem. Sci.* **2015**, *6*, 3868.
37. G. Kovacs, S. M. Kozlov, K. M. Neyman, *J. Phys. Chem. C* **2017**, *121*, 10803.
38. G. Guisbiers, *Adv. Phys. X* **2019**, *4*, 1668299.
39. K. M. Neyman, S. M. Kozlov, *NPG Asia Mater.* **2022**, *14*, 1.
40. S. M. Kozlov, K. M. Neyman, *Top. Catal.* **2013**, *56*, 867.
41. P. Grammatikopoulos, *Curr. Opin. Chem. Eng.* **2019**, *23*, 164.
42. M. Bohra, P. Grammatikopoulos, V. Singh, J. Zhao, E. Toulkeridou, S. Steinhauer, J. Kioseoglou, J.-F. Bobo, K. Nordlund, F. Djurabekova, M. Sowwan, *Phys. Rev. Mater.* **2017**, *1*, 066001.
43. S. A. Davari, D. Mukherjee, *AIChE J.* **2018**, *64*, 18.
44. K. Yasuoka, M. Matsumoto, *J. Chem. Phys.* **1998**, *109*, 8451.
45. G. Chkonia, J. Wölk, R. Strey, J. Wedekind, D. Reguera, *J. Chem. Phys.* **2009**, *130*, 064505.
46. H. C. Andersen, *J. Chem. Phys.* **1980**, *72*, 2384.
47. I. Chepkasov, Y. Y. Gafner, S. Gafner, S. Bardakhanov, *Bull. Mater. Sci.* **2015**, *38*, 701.
48. I. Chepkasov, Y. Y. Gafner, S. Gafner, *Phase Transitions* **2017**, *90*, 590.
49. Y. Y. Gafner, S. L. Gafner, D. A. Ryzkova, A. V. Nomoev, *Beil. J. Nanotechnol.* **2021**, *12*, 72.
50. I. Chepkasov, Y. Y. Gafner, K. Zobov, S. Batoroev, S. Bardakhanov, *IOP Conference Series: Materials Science and Engineering*, vol. 110. IOP Publishing, **2016**, 012020.
51. S. Nosé, *J. Chem. Phys.* **1984**, *81*, 511.
52. W. G. Hoover, *Phys. Rev. A* **1985**, *31*, 1695.
53. P. Krasnochtchekov, K. Albe, Y. Ashkenazy, R. Averback, *J. Chem. Phys.* **2005**, *123*, 154314.
54. A. Vorontsov, B. Gel'chinskii, A. Korenchenko, *J. Exp. Theor. Phys.* **2012**, *115*, 789.
55. J. Zhao, V. Singh, P. Grammatikopoulos, C. Cassidy, K. Aranishi, M. Sowwan, K. Nordlund, F. Djurabekova, *Phys. Rev. B* **2015**, *91*, 035419.
56. M. Abbaspour, H. Akbarzadeh, Z. Valizadeh, *Inorg. Chem. Front.* **2018**, *5*, 1445.
57. J.-G. Mattei, P. Grammatikopoulos, J. Zhao, V. Singh, J. Vernieres, S. Steinhauer, A. Porkovich, E. Danielson, K. Nordlund, F. Djurabekova, M. Sowwan, *Chem. Mater.* **2019**, *31*, 2151.
58. D. Kim, C. Xie, N. Becknell, Y. Yu, M. Karamad, K. Chan, E. J. Crumlin, J. K. Nørskov, P. Yang, *J. Am. Chem. Soc.* **2017**, *139*, 8329.
59. J. Yan, B. K. Teo, N. Zheng, *Acc. Chem. Res.* **2018**, *51*, 3084.
60. B. Talukdar, T.-C. Kuo, B. T. Sneed, L.-M. Lyu, H.-M. Lin, Y.-C. Chuang, M.-J. Cheng, C.-H. Kuo, *ACS Appl. Mater. Interfaces* **2021**, *13*, 51839.
61. G. Zagler, M. Reticcioli, C. Mangler, D. Scheinecker, C. Franchini, J. Kotakoski, *2D Materials* **2020**, *7*, 045017.
62. J.-Q. Goh, J. Akola, R. Ferrando, *J. Phys. Chem. C* **2017**, *121*, 10809.
63. S. Lysgaard, J. S. Mørdal, H. A. Hansen, T. Vegge, *Phys. Chem. Chem. Phys.* **2015**, *17*, 28270.
64. N. Zanganeh, V. K. Guda, H. Toghiani, J. M. Keith, *ACS Appl. Mater. Interfaces* **2018**, *10*, 4776.
65. S. Plimpton, *J. Comput. Phys.* **1995**, *117*, 1.
66. S. Foiles, M. Baskes, M. S. Daw, *Phys. Rev. B* **1986**, *33*, 7983.
67. L. Zhang, Q. Li, S. Tian, G. Hong, *J. Nanomater.* **2019**, *2019*, 7612805.
68. L. J. Sham, W. Kohn, *Phys. Rev.* **1966**, *145*, 561.
69. P. Hohenberg, W. Kohn, *Phys. Rev.* **1964**, *136*, B864.
70. B. Hammer, L. B. Hansen, J. K. Nørskov, *Phys. Rev. B* **1999**, *59*, 7413.
71. G. Kresse, J. Hafner, *J. Phys.: Condens. Matter* **1994**, *6*, 8245.
72. G. Kresse, J. Hafner, *Phys. Rev. B* **1994**, *49*, 14251.
73. G. Kresse, J. Furthmüller, *Phys. Rev. B* **1996**, *54*, 11169.
74. P. E. Blöchl, *Phys. Rev. B* **1994**, *50*, 17953.
75. S. Grimme, J. Antony, S. Ehrlich, H. Krieg, *J. Chem. Phys.* **2010**, *132*, 154104.
76. G. Henkelman, B. P. Uberuaga, H. Jónsson, *J. Chem. Phys.* **2000**, *113*, 9901.
77. A. Stukowski, *Modell. Simul. Mater. Sci. Eng.* **2009**, *18*, 015012.
78. K. Momma, F. Izumi, *J. Appl. Crystallogr.* **2008**, *41*, 653.
79. K. Momma, F. Izumi, *J. Appl. Crystallogr.* **2011**, *44*, 1272.
80. P. Krasnochtchekov, K. Albe, R. Averback, *Int. J. Mater. Res.* **2003**, *94*, 1098.
81. A. E. Korenchenko, A. G. Vorontsov, B. R. Gel'chinskii, *High Temp.* **2016**, *54*, 229.
82. A. E. Korenchenko, A. G. Vorontsov, B. R. Gelchinski, G. P. Sannikov, *Phys. A* **2018**, *496*, 147.
83. J. Lee, J. Yang, S. G. Kwon, T. Hyeon, *Nat. Rev. Mater.* **2016**, *1*, 1.
84. R. L. McGraw, P. M. Winkler, P. E. Wagner, *Sci. Rep.* **2017**, *7*, 16896.
85. W. Z. Polak, *Chem. Phys. Lett.* **2016**, *659*, 263.
86. A. Stukowski, *Modell. Simul. Mater. Sci. Eng.* **2012**, *20*, 045021.
87. X.-N. Li, Z. Yuan, S.-G. He, *J. Am. Chem. Soc.* **2014**, *136*, 3617.
88. J.-J. Chen, X.-N. Li, Q. Chen, Q.-Y. Liu, L.-X. Jiang, S.-G. He, *J. Am. Chem. Soc.* **2018**, *141*, 2027.
89. W. Tang, E. Sanville, G. Henkelman, *J. Phys.: Condens. Matter* **2009**, *21*, 084204.
90. A. Patra, J. E. Bates, J. Sun, J. P. Perdew, *Proc. Natl. Acad. Sci. USA* **2017**, *114*, E9188.
91. Y. Suchorski, S. M. Kozlov, I. Bespalov, M. Datler, D. Vogel, Z. Budinska, K. M. Neyman, G. Rupprechter, *Nat. Mater.* **2018**, *17*, 519.

92. L. Ma, J. Akola, *Phys. Chem. Chem. Phys.* **2019**, *21*, 11351.
93. D. Tang, J. Zhang, *Rsc Adv.* **2013**, *3*, 15225.
94. L. Ma, M. Melander, K. Laasonen, J. Akola, *Phys. Chem. Chem. Phys.* **2015**, *17*, 7067.
95. C. Jia, G. Zhang, W. Zhong, J. Jiang, *ACS Appl. Mater. Interfaces* **2016**, *8*, 10315.
96. M. H. Weng, S. P. Ju, *J. Phys. Chem. C* **2012**, *116*, 18803.
97. W. T. Wallace, R. L. Whetten, *J. Am. Chem. Soc.* **2002**, *124*, 7499.
98. A. Lyalin, T. Taketsugu, *J. Phys. Chem. Lett.* **2010**, *1*, 1752.
99. V. P. Zhdanov, B. Kasemo, *Surf. Sci. Rep.* **1994**, *20*, 113.
100. S. Jiao, X. Fu, H. Huang, *Adv. Funct. Mater.* **2022**, *32*, 2107651.
101. X. Wang, G. Zhang, L. Yang, E. Sharman, J. Jiang, *Wiley Interdiscip. Rev.: Comput. Mol. Sci.* **2018**, *8*, e1369.
102. J. S. Hummelshøj, F. Abild-Pedersen, F. Studt, T. Bligaard, J. K. Nørskov, *Angew. Chem. Int. Ed.* **2012**, *51*, 272.
103. L. Falivene, S. M. Kozlov, L. Cavallo, *ACS Catal.* **2018**, *8*, 5637.
104. T. R. Munter, T. Bligaard, C. H. Christensen, J. K. Nørskov, *Phys. Chem. Chem. Phys.* **2008**, *10*, 5202.
105. Y. Zhang, S. Li, C. Sun, P. Wang, Y. Yang, D. Yi, X. Wang, J. Yao, *ACS Catal.* **2022**, *12*, 9201.
106. S. M. Kozlov, K. M. Neyman, *J. Catal.* **2016**, *337*, 111.
107. B. Pascucci, G. S. Otero, P. G. Belelli, M. M. Branda, *Appl. Surf. Sci.* **2019**, *489*, 1019.
108. S. Wehner, P. Hoffmann, D. Schmeisser, H. R. Brand, J. Küppers, *Chem. Phys. Lett.* **2006**, *423*, 39.
109. L. Kunz, F. M. Kuhn, O. Deutschmann, *J. Chem. Phys.* **2015**, *143*, 044108.
110. M. Jørgensen, H. Gronbeck, *ACS Catal.* **2019**, *9*, 8872.

SUPPORTING INFORMATION

Additional supporting information can be found online in the Supporting Information section at the end of this article.

How to cite this article: I. V. Chepkasov, V. S. Baidyshev, A. A. Golubnichiy, I. S. Zamulin, A. G. Kvashnin, S. M. Kozlov, *Aggregate* **2022**, *3*, e273. <https://doi.org/10.1002/agt2.273>